



Article

An Investigation of the Ice Cloud Detection Sensitivity of Cloud Radars Using the Raman Lidar at the ARM SGP Site

Mingcheng Wang ^{1,*} , Kelly A. Balmes ^{2,3}, Tyler J. Thorsen ⁴ , Dylan Willick ⁵ and Qiang Fu ¹¹ Department of Atmospheric Sciences, University of Washington, Seattle, WA 98195, USA; qfu@uw.edu² Cooperative Institute for Research in Environmental Sciences, University of Colorado Boulder, Boulder, CO 80303, USA; kelly.balmes@noaa.gov³ NOAA Global Monitoring Laboratory, Boulder, CO 80305, USA⁴ NASA Langley Research Center, Hampton, VA 23681, USA; tyler.thorsen@nasa.gov⁵ Carleton College, Northfield, MN 55057, USA; willickd@carleton.edu

* Correspondence: wmingch@uw.edu

Abstract: The ice cloud detection sensitivity of the millimeter cloud radar (MMCR) and the Ka-band Zenith radar (KAZR) is investigated using a collocated Raman lidar (RL) at the Atmospheric Radiation Measurement Program Southern Great Plains site. Only profiles that are transparent to the RL with ice clouds only are considered in this study. The MMCR underestimates the RL ice cloud optical depth (COD) by 20%. The MMCR detects no ice clouds in 37% of the profiles. These profiles where ice cloud goes undetected by the MMCR typically contain very optically thin clouds, with a mean RL ice COD of 0.03. Higher ice cloud detection sensitivity is found for the KAZR, which underestimates the RL ice COD by 15%. The decrease in the ice COD bias for the KAZR compared to the MMCR is largely due to a decrease in the ice COD bias for the situation where the transparent profiles with ice clouds are detected by both the RL and cloud radar. The climatic net ice cloud radiative effects (CREs) from the RL at the top of the atmosphere (TOA) and the surface are 3.2 W m^{-2} and -0.6 W m^{-2} , respectively. The ice CREs at the TOA and surface are underestimated for the MMCR by 0.7 W m^{-2} and 0.16 W m^{-2} (21% and 29%) and underestimated for the KAZR by 0.6 W m^{-2} and 0.14 W m^{-2} (17% and 24%). The ice clouds undetected by the cloud radars led to underestimating the climatic net cloud heating rates below 150 hPa by about $0\text{--}0.04 \text{ K day}^{-1}$.

Keywords: ice cloud; Raman lidar; cloud radar; cloud radiative effects; radiative transfer model

Citation: Wang, M.; Balmes, K.A.; Thorsen, T.J.; Willick, D.; Fu, Q. An Investigation of the Ice Cloud Detection Sensitivity of Cloud Radars Using the Raman Lidar at the ARM SGP Site. *Remote Sens.* **2022**, *14*, 3466. <https://doi.org/10.3390/rs14143466>

Academic Editor: Michael Obland

Received: 21 May 2022

Accepted: 14 July 2022

Published: 19 July 2022

Publisher's Note: MDPI stays neutral with regard to jurisdictional claims in published maps and institutional affiliations.



Copyright: © 2022 by the authors. Licensee MDPI, Basel, Switzerland. This article is an open access article distributed under the terms and conditions of the Creative Commons Attribution (CC BY) license (<https://creativecommons.org/licenses/by/4.0/>).

1. Introduction

Ice clouds cover 20–30% of the globe and strongly impact the weather and climate processes through their effects on the global radiative energy budget [1–8]. The ice cloud radiative effects (CREs) are closely related to ice cloud optical properties [9–12]. Thus, accurate and long-term measurements of ice cloud detection and optical properties are important in understanding the impact of ice clouds on the climate [13–15].

Ground-based remote sensing provides near-continuous cloud measurements and has been widely used to investigate cloud properties and evaluate satellite observations [16–24]. The Atmospheric Radiation Measurement (ARM) Southern Great Plains (SGP) site, located in Lamont, Oklahoma, is heavily instrumented, including the Raman lidar (RL) [25–27] and the millimeter cloud radar (MMCR) [28–31] and the Ka-band Zenith radar (KAZR) [32]. The RL operates at 355 nm and thus can detect all types of hydrometeors when the lidar beam can penetrate to the locations of hydrometeors. The lidar beam, however, can become fully attenuated during the period with optically thick clouds, which are not uncommon [27]. On the other hand, the millimeter-wavelength radar can penetrate all cloud types (except during periods of very heavy rains) but have lower detection sensitivities, thus leaving some clouds undetected, especially those with small cloud optical depth (COD) [28,29,32,33]. Borg et al. [34] investigated the sensitivity of the MMCR to optically thin single-layer ice

clouds at the ARM SGP site using three years of collocated RL observations. Borg et al. [34] found the MMCR only detected about 70% of the ice cloud with cloud optical depth (COD) smaller than 2, and the missed COD resulted in the longwave (LW) top of atmosphere (TOA) flux biases as large as -100 W m^{-2} . Note that Borg et al. [34] did not apply the multiple scattering correction, which may induce low biases for extinction profiles and, thus, COD derived from the RL.

In this study, we investigate the sensitivity of cloud radars to ice clouds using the RL, with a longer period from August 2008 to December 2014 than that in Borg et al. [34]. The RL observations considered are from the feature detection and extinction retrieval (FEX) value-added product (VAP) developed by Thorsen et al. [35] and Thorsen and Fu [36], which provides complementary depictions of cloud locations and explicitly considers the multiple scattering effects via a multiple scattering model in contrast to Borg et al. [34]. The Active Remote Sensing of Clouds (ARSCL) value-added product (VAP), which combines data from active remote sensors, has been widely used to investigate cloud properties as well as to quantify and assess CREs. As the successor to the retired MMCR, KAZR uses a new digital receiver that provides higher spatial and temporal resolutions than the MMCR [32]. This study investigates the sensitivity of both MMCR and KAZR ARSCL VAPs to ice clouds using collocated RL retrievals at the SGP site from August 2008 to December 2014. In addition, a radiative transfer model is used to investigate the impact of ice clouds that are undetected by the cloud radars on the TOA and surface radiative energy budget and atmospheric radiative heating rates. We seek to discriminate the differences in ice cloud properties observed by different instruments with different techniques, which can help better constrain the observed ice cloud properties and understand the impact of ice clouds on the weather and climate.

Section 2 describes the RL, MMCR, and KAZR data, and radiative transfer model used in this study. The main results are presented in Section 3, and Section 4 presents a summary and concluding remarks.

2. Data and Model

2.1. Raman Lidar and Cloud Radars

The ARM RL operates at 355 nm during the nighttime and daytime [25–27]. The FEX algorithm [17,35,36] is applied to the RL observations for feature masks (i.e., aerosol, liquid cloud, ice cloud, rain, etc.) and cloud extinction vertical profile retrieval. The RL data used in this study are at a 10 min temporal resolution and 30 m vertical resolution from August 2008 to December 2014 at the SGP site (36.61°N, 97.49°W). Same as Borg et al. [34], we only consider the subset of RL profiles where the lidar beam is not fully attenuated. The RL profiles where the lidar beam is not fully attenuated are referred to as transparent. Transparent profiles are defined as those where the signal-to-noise ratio is greater than one at 16 km [35,36]. Those fully attenuated are referred to as opaque cloudy-sky, and other RL profiles with aerosols only and without hydrometeors (i.e., ice cloud, liquid cloud, and rain) are referred to as clear-sky.

The MMCR is a zenith-pointing radar that operates at a frequency of 35 GHz [28,29]. It can provide the detection of hydrometeor reflectivity as low as -50 dBz up to 20 km above the ground. MMCR has a temporal and vertical resolution of 10 s and 43 m. The KAZR replaced the MMCR and is equipped with a new digital receiver with higher temporal (4 s) and vertical (30 m) resolutions than the MMCR [32]. In addition, the spectral artifacts for the KAZR are reduced substantially, allowing researchers to investigate cloud dynamics much more closely than with the MMCR.

We use the ARSCL VAP of the MMCR [29] from August 2008 to January 2011 and the KAZR [32] from January 2011 to December 2014. It should be noted that the top and bottom heights of hydrometeors used in this study in the ARSCLs VAP of MMCR and KAZR are based on combined radar and micropulse lidar observations. To compare MMCR/KAZR with the RL, we consider one vertical observational profile of MMCR/KAZR closest

to the RL observation time (i.e., the central time of a ± 5 min interval) for each RL profile considered.

In this study, the feature masks (e.g., ice cloud) and extinction profiles from the RL, and the top and bottom heights of hydrometeor layers in the ARSCL VAP of the MMCR and KAZR are used. The top and bottom heights of ice clouds from the RL are obtained from the RL features masks. The purpose of this study is to evaluate the impact of ice clouds that are not detected by MMCR/KAZR but by RL. Thus, for the MMCR and KAZR ice COD, the RL extinction profile is used but only at heights where the cloud radars detected ice clouds.

2.2. Radiative Transfer Model

This study uses the NASA Langley Fu-Liou radiative transfer (RT) model [9,37–41]. The model is based on the delta-four stream scheme for RT and the correlated k-distribution method for nongray gaseous, with 18 shortwave (SW) bands and 12 longwave bands.

We follow Wu et al. [42] and Balmes and Fu [43] to set up the RT model inputs. The temperature and water vapor profiles are from radiosondes, interpolated to the RL-FEX vertical resolution [35,36]. The water vapor profiles from radiosondes are scaled using the microwave radiometer (MWR) integrated water vapor measurements [44,45], centered on the RL observation time for a 2 min interval. We smooth the temperature and water vapor profiles using a running average of ± 300 m (i.e., average 20 vertical bins). The smoothed temperature and water vapor profiles, which are up to 16 km, are extended to 1 hPa using the ERA-Interim [46] seasonal climatology profiles over the SGP site, following Yang et al. [47]. In addition, the ERA-Interim ozone seasonal climatology profiles and National Oceanic and Atmospheric Administration (NOAA) Global Monitoring Laboratory observations of CO₂, N₂O, CH₄, and CFCs concentrations are used as model input.

The MODIS MCD43C1 Version 6 Bidirectional Reflectance Distribution Function and Albedo Model Parameters data set [48,49] are used for surface albedo. We linearly interpolate the monthly mean surface albedo from seven spectral bands to the model wavelengths; the values of the closest observational wavelengths are used for the model wavelengths outside the MODIS spectral bands [42,43]. The total sky albedo combines the black-sky and white-sky albedo weighted by the diffuse ratio. Following Schaaf et al. [49], the black-sky albedo is calculated as a function of the solar zenith angle. The diffuse ratio is initially derived from the empirical equation of Roesch et al. [48], which is a function of the solar zenith angle. The diffuse ratio is derived from the surface SW diffuse and direct components calculated by the RT model. The RT model is then run again with the updated diffuse ratio. For reference, with the updated diffuse ratio, the annual mean broadband total-sky, white-sky, and black-sky albedo at the SGP site from August 2008 to December 2014 are 0.20, 0.21, and 0.19, respectively. The AERONET monthly mean aerosol optical depth, single scattering albedo, asymmetry factor, and RL scale height at the SGP site are used.

For each RL transparent profile, the RL extinction profile is inputted. The ice cloud effective diameter is derived as a function of temperature following Heymsfield et al. [50]. For SW calculations, we run the RT model with the diurnal cycle of solar zenith angle from sunrise to sunset at an interval of 30 min, following Wu et al. [42] and Balmes and Fu [43]. For LW calculations, only one RT simulation is considered. The same RT simulations but with the MMCR or KAZR ice clouds are also performed. To simulate the MMCR and KAZR ice clouds, the RL extinction profile is inputted again but only at heights where the cloud radars detected ice clouds. We define the downward (upward) fluxes as positive (negative), and the CREs at the TOA and surface are defined as

$$CRE = \left[F^{\downarrow} - F^{\uparrow} \right]_{cloud} - \left[F^{\downarrow} - F^{\uparrow} \right]_{clear-sky} \quad (1)$$

The daily-mean SW CRE is calculated as

$$CRE = \frac{1}{t_{day}} \int_{sunrise}^{sunset} CRE(t) dt \quad (2)$$

where $CRE(t)$ is the instantaneous CRE at a given time t and t_{day} is the time in a day (i.e., 86,400 s); the LW CRE from the LW RT simulation is then the daily-mean LW CRE. Positive CRE represents a warming effect, and negative CRE represents a cooling effect.

The average daily-mean CREs weighted by the occurrence fraction of RL transparent profiles with ice clouds only (see Section 3.1 below) are provided as the climatic CREs of ice clouds considered in this study. Since the ice clouds could also occur with liquid clouds in a profile, the climatic ice CREs and the climate impact of the ice clouds undetected by the MMCR/KAZR from this study are on their conservative sides.

3. Results

3.1. Cloud Occurrence Fraction

Figure 1 shows examples of hydrometeors detected by the RL and the MMCR. On 8 September 2008 (Figure 1a), there were periods of clear-sky before 2 UTC and a period of opaque cloudy-sky after 12 UTC, related to the RL's attenuation due to precipitation; transparent profiles occurred before 12 UTC, which corresponded to the outflow of convective clouds. On 28 October 2009 (Figure 1b), there were periods of opaque cloudy-sky from 15–17 UTC and after 20 UTC; the remaining times were transparent with clouds from 6 to 12 km. Consistent with Borg et al. [34], a significant portion of the ice clouds, especially the uppermost parts, are missed by the MMCR, whereas the ice clouds are detected by the RL (blue in Figure 1).

The occurrence fraction of clear-sky and opaque cloudy-sky at the SGP site from the RL is shown in Figure 2. There are 315,224 total RL profiles from August 2008 to December 2014. The clear-sky and opaque cloudy-sky occurrence fractions are 0.39 and 0.31, which is in good agreement with Balmes and Fu [43] (see their Figure 2). Note that the small differences in occurrence fractions in this study compared with Balmes and Fu [43] are due to difference in the time period considered. Based on the RL feature mask [35,36], we partition the transparent profiles into those with ice clouds only (pink in Figure 2) and others (e.g., including both ice and liquid clouds or only liquid clouds, for a given profile) (green in Figure 2). In this study, we only consider the transparent profiles with ice clouds only, which have an occurrence fraction of 0.20. The transparent profiles with ice clouds only are further partitioned into profiles including ice clouds detected by both RL and cloud radar and profiles detected by the RL only. Hereafter, the 'transparent profiles' refer to the transparent profiles with ice clouds only, unless otherwise indicated.

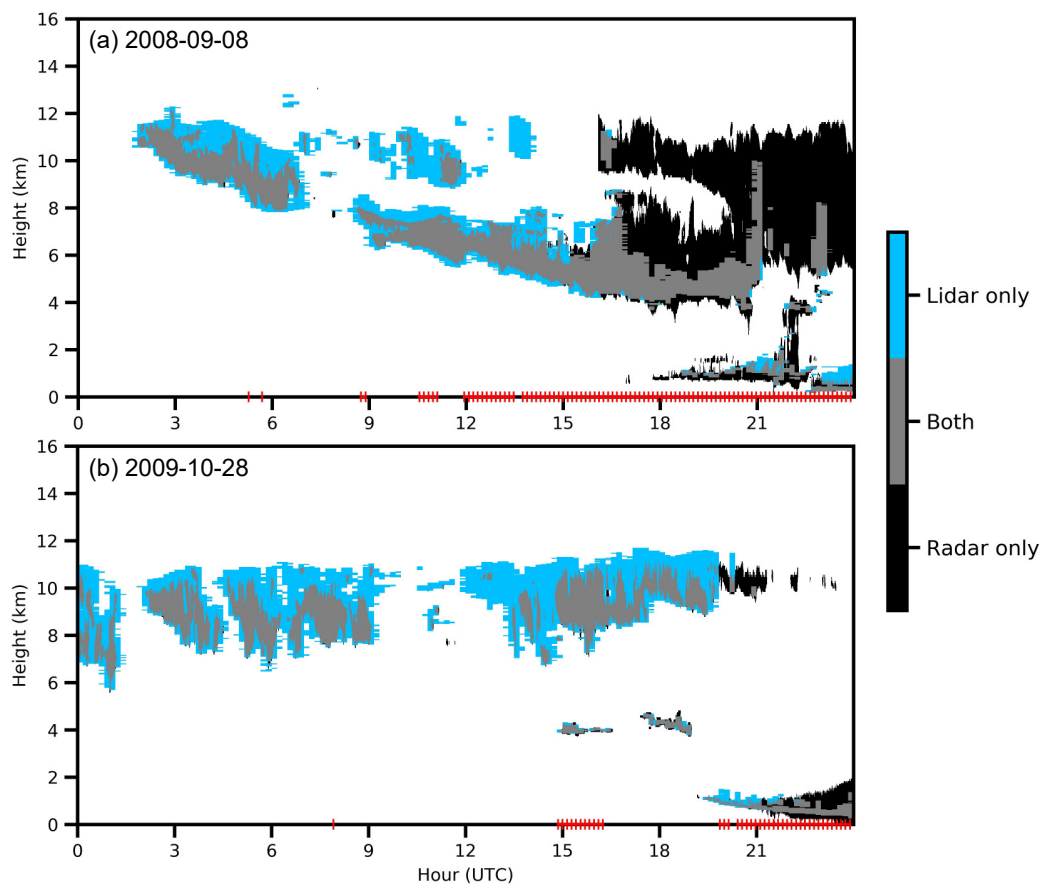


Figure 1. Raman lidar (RL) and millimeter wavelength cloud radar (MMCR) observations on (a) 8 September 2008 and (b) 28 October 2009 at the Southern Great Plains (SGP) site. The hydrometeors detected by the RL and MMCR are shown. The hydrometeors observed by both RL and MMCR (i.e., both) are shown in gray, those observed by RL only (i.e., lidar only) are shown in light blue, and those observed by MMCR only (i.e., radar only) are shown in black. The periods when the RL was fully attenuated are indicated as red “+” along the x-axis.

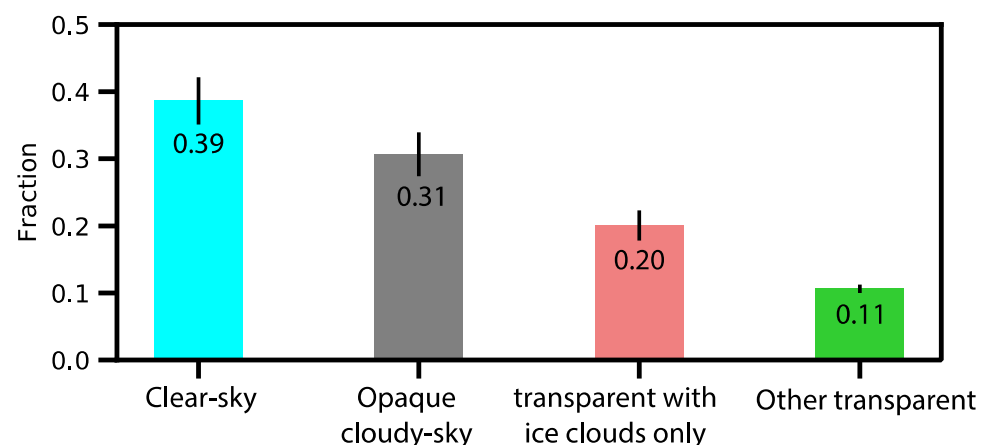


Figure 2. Clear-sky (cyan) and cloud occurrence fractions for the Raman lidar (RL) over at the Southern Great Plains (SGP) site from August 2008 to December 2014. The cloud occurrence fraction is partitioned into opaque cloudy-sky (gray) and transparent to the RL. The transparent fraction is further partitioned into transparent with ice clouds only (pink) and other transparent (green). The fraction values are labeled within each bar. The error bars are the corresponding one standard deviation of annual-mean fraction values from January 2009 to December 2014.

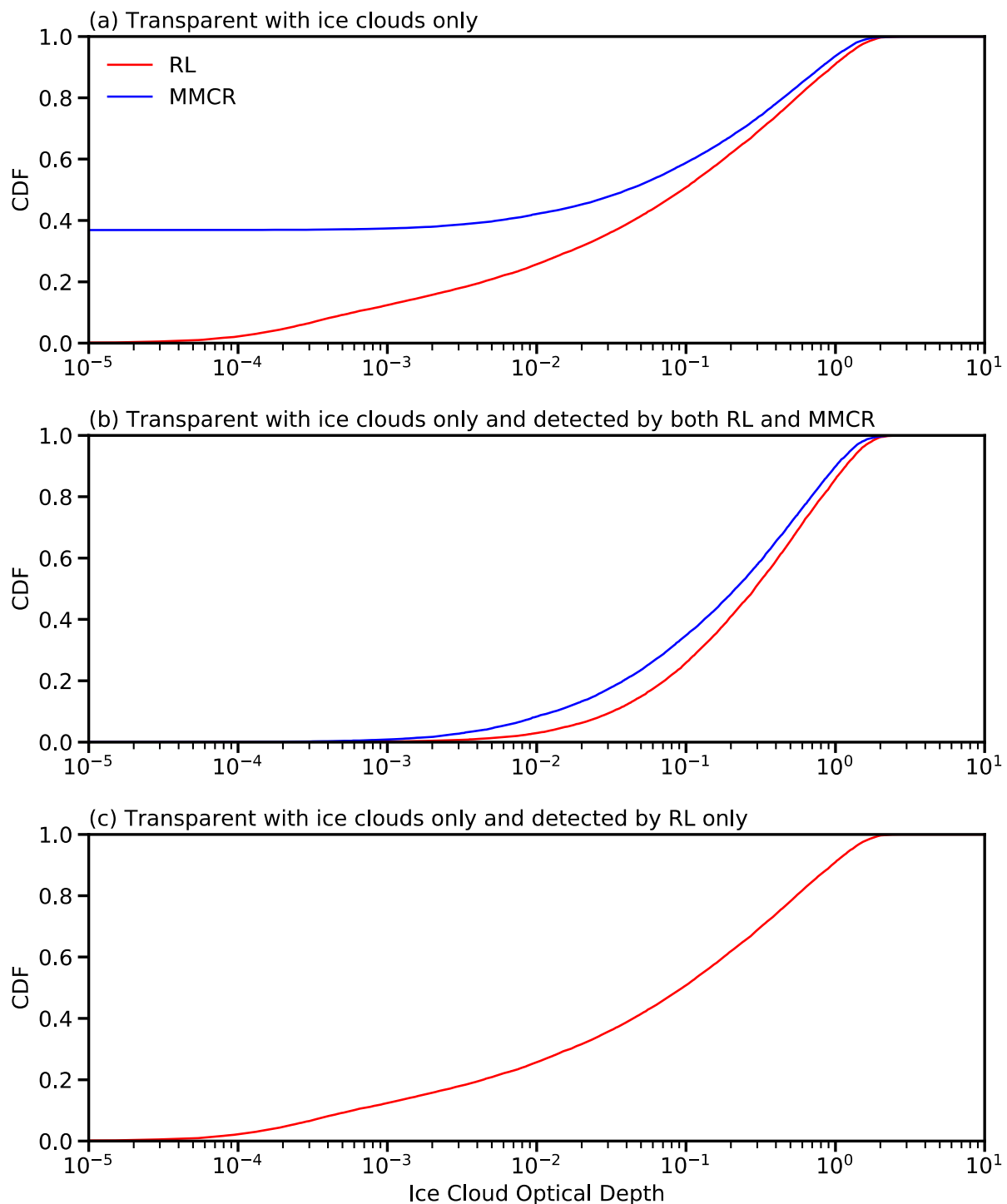


Figure 3. Cumulative distribution functions (CDFs) of ice cloud optical depth from the Raman lidar (RL; red) and millimeter wavelength cloud radar (MMCR; blue) observations at the Southern Great Plains (SGP) site from August 2008 to January 2011. The observations are shown for profiles that are (a) transparent with ice clouds only, (b) transparent with ice clouds only and detected by both RL and MMCR, and (c) transparent with ice clouds only and detected by RL only. In (c), no ice clouds are detected by MMCR, and thus only the RL result is shown here.

Table 2 is the same as Table 1, but for the RL and KAZR from January 2011 to December 2014. The CDFs of ice COD for the KAZR compared to the CDFs for RL ice COD (Figure S1) are quite similar to the MMCR and RL ice COD comparison (Figure 3). The mean RL

ice COD from January 2011 to December 2014 is 0.31, which is almost identical to the RL mean value from August 2008 to January 2014 (i.e., 0.30 in Table 1). KAZR underestimates the mean RL ice COD by 15%, which is a decrease in the bias as compared to the MMCR (Table 1). Interestingly, the decrease in the bias is largely due to a decrease in the ice COD bias for the situation where the ice clouds are detected by both RL and cloud radar, as the mean RL ice COD was underestimated by 11% for KAZR (Table 2) compared to an underestimation of 18% for MMCR (Table 1). Such improvement in ice cloud detections for the KAZR versus the MMCR may be related to the KAZR's better detection sensitivity [32]. On the other hand, the percentage of ice cloud profiles undetected by KAZR is 37% (Table 2), which is almost identical to the percentage of ice clouds undetected by MMCR (36.9%; Table 1).

Table 2. Same as Table 1, but for the Raman lidar (RL) and Ka-band ARM Zenith Radar (KAZR) observations at the Southern Great Plains (SGP) site from January 2011 to December 2014.

	COD	SW TOA CRE (W m ⁻²)		LW TOA CRE (W m ⁻²)		Net TOA CRE (W m ⁻²)		SW SFC CRE (W m ⁻²)		LW SFC CRE (W m ⁻²)		Net SFC CRE (W m ⁻²)	
Transparent with ice clouds only													
RL	0.31	-6.92	(-1.39)	23.17	(4.65)	16.24	(3.26)	-7.39	(-1.48)	4.48	(0.9)	-2.93	(-0.59)
KAZR	0.26	-5.66	(-1.14)	19.09	(3.83)	13.42	(2.69)	-6.2	(-1.24)	3.99	(0.8)	-2.22	(-0.45)
KAZR-RL	-0.05	1.26	(0.25)	-4.09	(-0.82)	-2.82	(-0.57)	1.19	(0.24)	-0.48	(-0.1)	0.71	(0.14)
(KAZR-RL)/RL	-14.9%	-18.3%		-17.6%		-17.4%		-16.1%		-10.8%		-24.2%	
Transparent with ice clouds only and detected by both RL and KAZR (63.0%)													
RL	0.47	-10.15	(-1.28)	34.28	(4.33)	24.12	(3.05)	-11.07	(-1.4)	6.85	(0.87)	-4.23	(-0.53)
KAZR	0.42	-8.98	(-1.14)	30.22	(3.82)	21.24	(2.69)	-9.84	(-1.24)	6.32	(0.8)	-3.51	(-0.44)
KAZR-RL	-0.05	1.18	(0.15)	-4.06	(-0.51)	-2.88	(-0.36)	1.24	(0.16)	-0.52	(-0.07)	0.71	(0.09)
(KAZR-RL)/RL	-11.2%	-11.6%		-11.8%		-11.9%		-11.2%		-7.6%		-16.9%	
Transparent with ice clouds only and detected by RL only (37.0%)													
RL	0.04	-1.41	(-0.1)	4.13	(0.31)	2.71	(0.2)	-1.12	(-0.08)	0.42	(0.03)	-0.7	(-0.05)
KAZR	0	0	(0)	0	(0)	0	(0)	0	(0)	0	(0)	0	(0)
KAZR-RL	-0.04	1.41	(0.1)	-4.13	(-0.31)	-2.71	(-0.2)	1.12	(0.08)	-0.42	(-0.03)	0.7	(0.05)
(KAZR-RL)/RL	—	—		—		—		—		—		—	

The CDFs of ice cloud base height, cloud top height, and cloud geometric depth from the RL and MMCR are shown in Figure 4. For the transparent profiles including ice clouds detected by both the RL and MMCR (Figure 4a–c), the mean ice cloud base and cloud top heights from the RL (MMCR) are 8.51 (9.02) and 11.21 (10.48) km, respectively, and the mean cloud geometric depth from the RL (MMCR) is 2.70 (1.46) km. Thus, the MMCR ice cloud geometric depth is 46% smaller than the RL ice cloud geometric depth. For the profiles where the ice clouds are detected by the RL only (Figure 4d–f), the mean ice cloud base height, cloud top height, and cloud geometric depth are 10.03, 11.15, and 1.11 km, which are thinner with higher cloud base as compared to those detected by both RL and MMCR. The CDFs of ice cloud base height, cloud top height, and cloud geometric depth from the RL and KAZR are shown in Figure S2. In line with the decrease in ice COD bias for the KAZR compared to the MMCR, the mean ice cloud geometric depth in the RL is underestimated in KAZR by 38% versus 46% in MMCR.

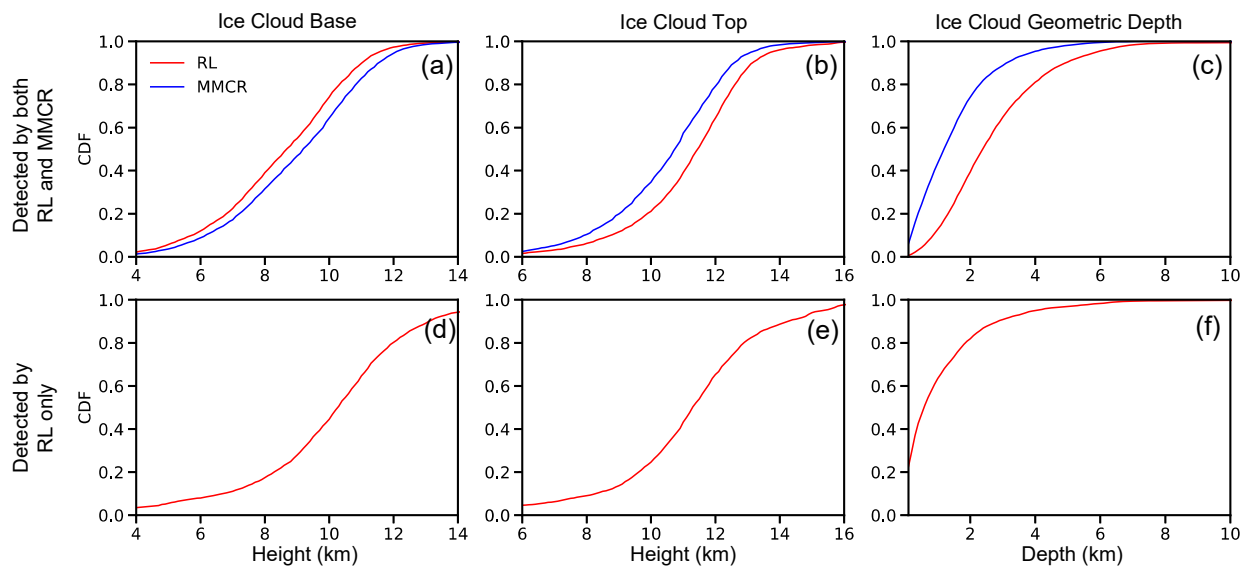


Figure 4. (a–c) Cumulative distribution functions (CDFs) of ice cloud base height (left), cloud top height (middle), and cloud geometric depth (right) (units: km) for transparent profiles with ice clouds only and detected by both Raman lidar (RL; red) and millimeter wavelength cloud radar (MMCR; blue) at the Southern Great Plains (SGP) site from August 2008 to January 2011. (d–f) CDFs for transparent profiles with ice clouds only that are detected by RL only; thus, only the RL results are shown here.

3.3. Ice CREs

In this subsection, we investigate the ice CREs. The SW, LW, and net CREs at the TOA and surface for transparent profiles detected by the RL with ice clouds only are shown in Table 1. The CDFs of CREs at the TOA (surface) are provided in Figure 5 (Figure 6). Results of the CREs for the RL compared to KAZR are given in Table 2; the CDFs for the KAZR and RL comparison are shown in Figures S3 and S4, which are very similar to the MMCR and RL comparison (Figures 5 and 6). The climatic CREs, which are the CREs weighted by the occurrence fraction of RL transparent profiles with ice clouds only (i.e., 0.20 in Figure 2), are also provided in Tables 1 and 2. The climatic CREs for those detected by both the RL and MMCR (KAZR) and those detected by RL only are provided, weighted by the fraction of transparent profiles with ice clouds only (i.e., 0.20) multiplied by their corresponding occurrence percentages, i.e., 63.1% and 36.9% (63.0% and 37.0%) in Table 1 (Table 2).

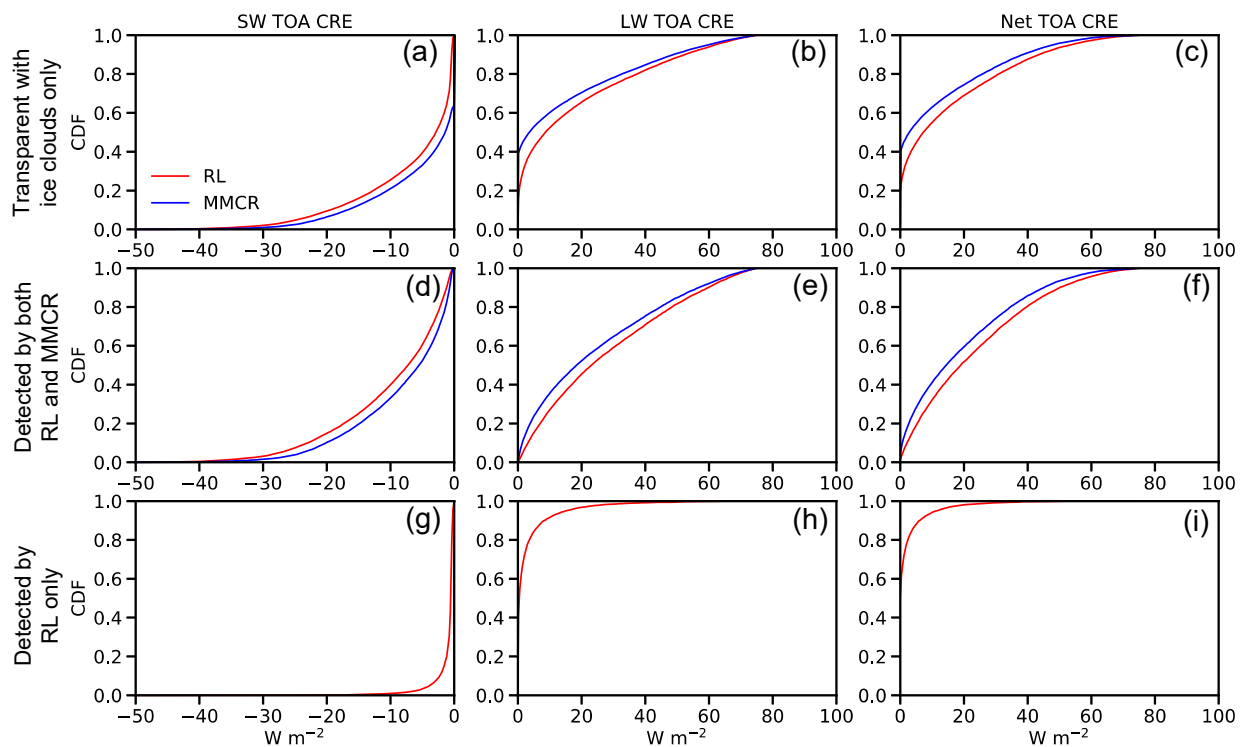


Figure 5. (a–c) Cumulative distribution functions (CDFs) of shortwave (SW) (left), longwave (LW) (middle), and net (right) daily-mean cloud radiative effects (CREs, units: $W m^{-2}$) at the top of atmosphere (TOA) for transparent profiles with ice clouds only that are detected by the Raman lidar (RL; red) and millimeter wavelength cloud radar (MMCR; blue) at the Southern Great Plains (SGP) site from August 2008 to January 2011. (d–f) CDFs for transparent profiles with ice clouds only and detected by both RL and MMCR. (g–i) CDFs for transparent profiles with ice clouds only that are detected by RL only; thus, only the RL results are shown here.

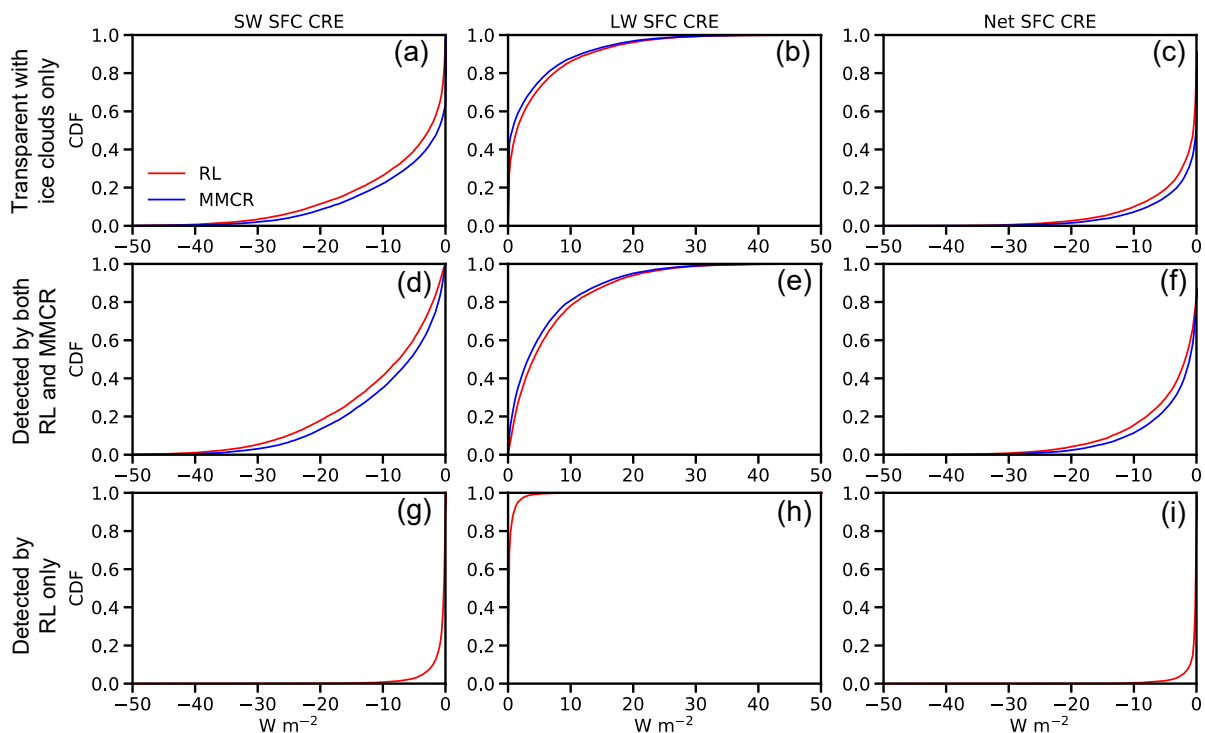


Figure 6. Same as Figure 5, but for the daily-mean cloud radiative effects (CREs) at the surface (SFC).

As mentioned before, for MMCR and KAZR, the RL extinction profile is used but only at heights where the cloud radars detected ice clouds; the ice cloud effective diameter for both the MMCR/KAZR and RL profiles are derived following Heymsfield et al. [50] by considering the radiosonde temperature profile. Therefore, the differences in ice CREs at the TOA and surface and radiative heating rates for the MMCR/KAZR versus RL, as will be shown later, are solely due to the ice clouds undetected by the cloud radar (i.e., Sections 3.1 and 3.2).

Consistent with previous studies, e.g., [3,9,51], ice clouds have negative SW CREs by reflecting more SW radiation back to space (Figures 5a,d,g and 6a,d,g) and positive LW CREs by reducing the outgoing LW radiation (Figures 5b,e,h and 6b,e,h) at both the TOA and surface. Interesting to note that the net CRE at the TOA is dominated by the LW CRE (Figure 5c,f,i), while the SW CRE dominates the net CRE at the surface (Figure 6c,f,i).

For the climatic values from August 2008 to January 2011 (Table 1), the SW, LW, and net CREs at the TOA (surface) from the RL are -1.4 , 4.5 , and 3.1 W m^{-2} (-1.4 , 0.9 , and -0.6 W m^{-2}), respectively. The differences of SW, LW, and net CREs at the TOA (surface) for the MMCR compared to the RL are 0.3 , -1.0 , and -0.7 W m^{-2} (0.3 , -0.1 , and 0.2 W m^{-2}), respectively. As compared to the CREs from the RL, the magnitudes of SW, LW, and net CREs from the MMCR are underestimated by 21–23% (15–29%) at the TOA (surface), which is a similar magnitude of the ice COD underestimation for the MMCR compared to the RL (i.e., 20%). Interestingly, 73–81% of the MMCR's CRE underestimation is due to the undetected ice clouds in profiles where ice clouds are detected by both the RL and MMCR. The remaining 19–27% of the MMCR's CRE underestimations are due to the profiles with optically very thin ice clouds only detected by the RL (Table 1).

The SW, LW, and net CREs at the TOA (surface) are underestimated by 17–18% (11–24%) for the KAZR compared to those from the RL (Table 2), which are all smaller as compared to the underestimation of MMCR (Table 1). As noted above, compared to the MMCR, the decrease in the underestimation of the ice COD for KAZR compared to the RL is due to the undetected ice clouds in profiles where ice clouds are detected by both the RL and radar. Here, we find 60–70% of the CRE underestimations for the KAZR compared to the RL is due to the undetected ice clouds in profiles where ice clouds are detected by both the RL and KAZR, and 30–40% is due to the profiles with optically very thin ice clouds detected by the RL only.

Figure 7 shows the profiles of SW, LW, and net cloud heating rates for transparent profiles with ice clouds only based on RL and MMCR observations and their differences. Again, the results for the KAZR compared to the RL are quite similar (see Figure S5 versus Figure 7). The SW cloud heating rates are positive between 150–400 hPa, with a peak of about 0.2 K day^{-1} at around 250 hPa. The SW cloud heating rates are negative, with values around -0.05 K day^{-1} below 400 hPa (Figure 7a). The LW cloud heating rates are positive below 150 hPa, with peaks of about 0.2 – 0.4 K day^{-1} around 250 hPa, and are negative with a magnitude of around 0.1 K day^{-1} above 150 hPa (Figure 7b). The shapes of the net cloud heating rates are similar to the LW cloud heating rates, with peaks of about 0.6 K day^{-1} around 250 hPa (Figure 7c). The undetected ice clouds by MMCR lead to SW, LW, and net cloud heating underestimations of 0 – 0.2 K day^{-1} below 150 hPa (0 – 0.04 K day^{-1} in the climatic sense), with peaks around 200–250 hPa. Above 150 hPa, the underestimation of LW and net cloud cooling is about 0.02 K day^{-1} .

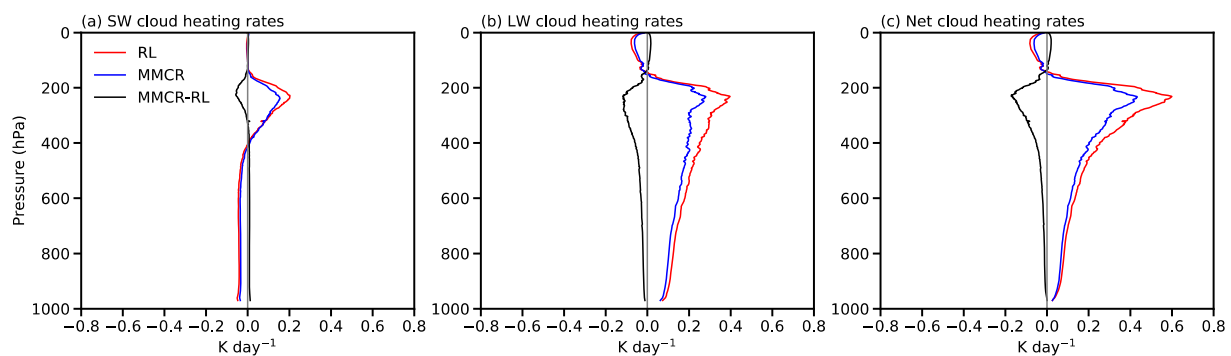


Figure 7. Mean profiles of (a) shortwave (SW), (b) longwave (LW), and (c) net daily-mean cloud heating rates (K day^{-1}) based on the Raman lidar (RL; red) and millimeter wavelength cloud radar (MMCR; blue) observations for transparent profiles with ice clouds only, and their differences (MMCR-RL; black) at the Southern Great Plains (SGP) site from August 2008 to January 2011.

4. Discussion and Conclusions

This study investigated ice clouds observed by cloud radars (i.e., MMCR and KAZR) and the collocated RL and their differences at the ARM SGP site between August 2008 and December 2014. Profiles that are transparent to the RL with ice clouds only are considered.

The mean RL ice COD for transparent profiles between August 2008 and January 2011 is 0.30, which is underestimated by the MMCR by 20%. The underestimation of ice COD for the MMCR versus the RL here is smaller than the MMCR underestimation ($\sim 30\%$) shown in Borg et al. [34]. Such discrepancy may be because we use ARSCLs VAP of MMCR in this study, i.e., the hydrometeors' top and bottom heights are based on combined radar and micropulse lidar observations. We find that the MMCR can only detect ice clouds in about 63% of the RL transparent profiles. The remaining profiles (37%) are comprised of optically very thin ice clouds that go undetected by the MMCR, with a mean RL ice COD of 0.03. A decrease in the underestimation of ice COD is found for the KAZR, which underestimates the RL ice COD by 15%. The decrease in the ice COD underestimation for KAZR compared to that from MMCR is largely due to a decrease in the ice COD bias for the situation where ice clouds are detected by both the RL and cloud radar. We also find a smaller underestimation of ice cloud depth for the KAZR, which underestimates the RL ice cloud depth (i.e., 2.7 km) by 38% instead of 46% by the MMCR, for the situation where the ice clouds are detected by both the RL and cloud radar.

We investigate the impacts of ice clouds on the TOA and surface radiative budget and radiative heating rate profiles using the NASA Langley Fu-Liou RT model. From August 2008 to January 2011, the climatic LW CRE from the RL at the TOA is 4.5 W m^{-2} , partly compensated by the negative SW CRE of -1.4 W m^{-2} , which overall leads to a positive net CRE of 3.1 W m^{-2} . On the other hand, the climatic SW CRE at the surface from the RL is -1.4 W m^{-2} , which is compensated by a positive LW CRE of 0.9 W m^{-2} , and ultimately yields a net CRE of -0.6 W m^{-2} . Compared to the RL, the CREs from the MMCR are underestimated by 21–23% at the TOA and 15–29% at the surface. About 73–81% of the CREs underestimation is due to cases detected by both the RL and MMCR, and those optically very thin ice clouds detected by RL only contribute 19–27% of the CREs underestimation by the MMCR.

The CRE underestimation is smaller for the KAZR: 17–18% at the TOA and 11–24% at the surface. The decrease in the CRE bias is due to a decrease in the ice COD bias. It is also interesting to note that the optically very thin ice clouds in profiles where the KAZR does not detect any clouds contribute 30–40% of the CREs underestimation for the KAZR compared to the RL, and 60–70% is due to the undetected ice clouds in profiles where ice clouds are detected by both RL and KAZR.

We find positive SW cloud radiative heating rates around 150–400 hPa, with a peak of 0.2 K day^{-1} at 250 hPa. Negative SW cloud radiative heating rates are found below

400 hPa. The LW cloud heating rates are positive below 150 hPa, with peaks of about $0.2\text{--}0.4\text{ K day}^{-1}$ at 250 hPa, and negative heating rates above 150 hPa. The net cloud heating rates are similar to the LW cloud heating rates, with peaks of 0.6 K day^{-1} at 250 hPa. The ice clouds undetected by the cloud radars lead to underestimating the SW, LW, and net cloud heating of about $0\text{--}0.2\text{ K day}^{-1}$ below 150 hPa, which is $0\text{--}0.04\text{ K day}^{-1}$ in the climatic sense.

This study presents the differences in ice cloud properties observed by different instruments with different techniques (i.e., RL and cloud radar), and their impacts on CREs at the TOA and surface and radiative heating rate profile. The sensitivity of the KAZR in terms of ice COD and its impact on CREs are also established in this study. To constrain ice cloud properties and better understand the impact of ice clouds on the weather and climate, it is of great significance to utilize various observations, including the cloud radar, lidar, and other equivalent observation platforms [52].

Supplementary Materials: The following supporting information can be downloaded at: <https://www.mdpi.com/article/10.3390/rs14143466/s1>, which shows the results for KAZR versus the RL.

Author Contributions: Conceptualization, M.W., K.A.B., T.J.T. and Q.F.; methodology, M.W., K.A.B. and Q.F.; software, M.W., K.A.B., D.W.; validation, M.W., K.A.B., T.J.T. and Q.F.; formal analysis, M.W., K.A.B. and D.W.; investigation, M.W., K.A.B., T.J.T., D.W. and Q.F.; resources, Q.F.; data curation, M.W., K.A.B. and D.W.; writing—original draft preparation, M.W.; writing—review and editing, M.W., K.A.B., T.J.T., D.W. and Q.F.; visualization, M.W., K.A.B. and D.W.; supervision, Q.F.; project administration, Q.F.; funding acquisition, Q.F. All authors have read and agreed to the published version of the manuscript.

Funding: This study is supported by the U.S. Department of Energy Office of Science (BER) under Grant DE-SC0020135.

Data Availability Statement: Data can be downloaded from the ARM data archive for the Raman lidar (<https://adc.arm.gov/discovery/#/results/s::rlproffex1thor>), cloud radar (MMCR: <https://adc.arm.gov/discovery/#/results/s::sgparscl1clothC>; KAZR: <https://adc.arm.gov/discovery/#/results/s::sgparsclkazr1kolliasC1>), and microwave radiometer (<https://adc.arm.gov/discovery/#/results/s::sgpmwrret1liljclouC1>), all accessed on 20 May 2022.

Acknowledgments: We would like to acknowledge the high-performance computing support from Cheyenne (doi:10.5065/D6RX99HX) provided by NCAR's Computational and Information Systems Laboratory, sponsored by the National Science Foundation, for the analyses presented in this study and for the data management, storage, and preservation. The authors thank the anonymous reviewers for their constructive comments that have helped improve the manuscript.

Conflicts of Interest: The authors declare no conflict of interest.

References

1. Berry, E.; Mace, G.G. Cloud properties and radiative effects of the Asian summer monsoon derived from A—Train data. *J. Geophys. Res. Atmos.* **2014**, *119*, 9492–9508. [CrossRef]
2. Dupont, J.-C.; Haeffelin, M. Observed instantaneous cirrus radiative effect on surface-level shortwave and longwave irradiances. *J. Geophys. Res. Atmos.* **2008**, *113*, D21202. [CrossRef]
3. Liou, K.-N. Influence of Cirrus Clouds on Weather and Climate Processes: A Global Perspective. *Mon. Weather Rev.* **1986**, *114*, 1167–1199. [CrossRef]
4. Lolli, S.; Campbell, J.R.; Lewis, J.R.; Gu, Y.; Marquis, J.W.; Chew, B.N.; Liew, S.-C.; Salinas, S.V.; Welton, E.J. Daytime Top-of-the-Atmosphere Cirrus Cloud Radiative Forcing Properties at Singapore. *J. Appl. Meteorol. Clim.* **2017**, *56*, 1249–1257. [CrossRef]
5. Sherwood, S.C. On moistening of the tropical troposphere by cirrus clouds. *J. Geophys. Res. Atmos.* **1999**, *104*, 11949–11960. [CrossRef]
6. Fu, Q.; Hu, Y.; Yang, Q. Identifying the top of the tropical tropopause layer from vertical mass flux analysis and CALIPSO lidar cloud observations. *Geophys. Res. Lett.* **2007**, *34*. [CrossRef]
7. Lin, L.; Fu, Q.; Zhang, H.; Su, J.; Yang, Q.; Sun, Z. Upward mass fluxes in tropical upper troposphere and lower stratosphere derived from radiative transfer calculations. *J. Quant. Spectrosc. Radiat. Transf.* **2013**, *117*, 114–122. [CrossRef]
8. Sun, W.; Baize, R.R.; Videen, G.; Hu, Y.; Fu, Q. A method to retrieve super-thin cloud optical depth over ocean background with polarized sunlight. *Atmos. Chem. Phys.* **2015**, *15*, 11909–11918. [CrossRef]

9. Fu, Q.; Liou, K.N. Parameterization of the Radiative Properties of Cirrus Clouds. *J. Atmos. Sci.* **1993**, *50*, 2008–2025. [[CrossRef](#)]
10. Heymsfield, A.J.; Krämer, M.; Luebke, A.; Brown, P.; Cziczo, D.J.; Franklin, C.; Lawson, P.; Lohmann, U.; McFarquhar, G.; Ulanowski, Z.; et al. Cirrus Clouds. *Meteorol. Monogr.* **2017**, *58*, 2.1–2.26. [[CrossRef](#)]
11. Platt, C.M.R.; Harshvardhan. Temperature dependence of cirrus extinction: Implications for climate feedback. *J. Geophys. Res. Atmos.* **1988**, *93*, 11051–11058. [[CrossRef](#)]
12. Zhang, Y.; Macke, A.; Albers, F. Effect of crystal size spectrum and crystal shape on stratiform cirrus radiative forcing. *Atmos. Res.* **1999**, *52*, 59–75. [[CrossRef](#)]
13. Fu, Q.; Baker, M.; Hartmann, D.L. Tropical cirrus and water vapor: An effective Earth infrared iris feedback? *Atmos. Chem. Phys.* **2002**, *2*, 31–37. [[CrossRef](#)]
14. Stephens, G.L.; Tsay, S.-C.; Stackhouse, P.W.; Flatau, P.J. The Relevance of the Microphysical and Radiative Properties of Cirrus Clouds to Climate and Climatic Feedback. *J. Atmos. Sci.* **1990**, *47*, 1742–1754. [[CrossRef](#)]
15. Waliser, D.E.; Li, J.-L.F.; Woods, C.P.; Austin, R.T.; Bacmeister, J.; Chern, J.; Del Genio, A.; Jiang, J.H.; Kuang, Z.; Meng, H.; et al. Cloud ice: A climate model challenge with signs and expectations of progress. *J. Geophys. Res. Atmos.* **2009**, *114*, D00A21. [[CrossRef](#)]
16. Balmes, K.A.; Fu, Q. An Investigation of Optically Very Thin Ice Clouds from Ground-Based ARM Raman Lidars. *Atmosphere* **2018**, *9*, 445. [[CrossRef](#)]
17. Balmes, K.A.; Fu, Q.; Thorsen, T.J. Differences in Ice Cloud Optical Depth From CALIPSO and Ground-Based Raman Lidar at the ARM SGP and TWP Sites. *J. Geophys. Res. Atmos.* **2019**, *124*, 1755–1778. [[CrossRef](#)]
18. Campbell, J.R.; Hlavka, D.L.; Welton, E.J.; Flynn, C.J.; Turner, D.D.; Spinhirne, J.D.; Scott, V.S.; Hwang, I.H. Full-Time, Eye-Safe Cloud and Aerosol Lidar Observation at Atmospheric Radiation Measurement Program Sites: Instruments and Data Processing. *J. Atmos. Ocean. Technol.* **2002**, *19*, 431–442. [[CrossRef](#)]
19. Comstock, J.M.; Ackerman, T.P.; Turner, D.D. Evidence of high ice supersaturation in cirrus clouds using ARM Raman lidar measurements. *Geophys. Res. Lett.* **2004**, *31*, L11106. [[CrossRef](#)]
20. Hollars, S.; Fu, Q.; Comstock, J.; Ackerman, T. Comparison of cloud-top height retrievals from ground-based 35 GHz MMCR and GMS-5 satellite observations at ARM TWP Manus site. *Atmos. Res.* **2004**, *72*, 169–186. [[CrossRef](#)]
21. Sassen, K.; Campbell, J.R. A Midlatitude Cirrus Cloud Climatology from the Facility for Atmospheric Remote Sensing. Part I: Macrophysical and Synoptic Properties. *J. Atmos. Sci.* **2001**, *58*, 481–496. [[CrossRef](#)]
22. Shupe, M.D.; Comstock, J.M.; Turner, D.D.; Mace, G.G. Cloud Property Retrievals in the ARM Program. *Meteorol. Monogr.* **2016**, *57*, 19.11–19.20. [[CrossRef](#)]
23. Thorsen, T.J.; Fu, Q.; Comstock, J. Comparison of the CALIPSO satellite and ground-based observations of cirrus clouds at the ARM TWP sites. *J. Geophys. Res. Atmos.* **2011**, *116*, D21203. [[CrossRef](#)]
24. Thorsen, T.J.; Fu, Q.; Comstock, J.M.; Sivaraman, C.; Vaughan, M.A.; Winker, D.M.; Turner, D.D. Macrophysical properties of tropical cirrus clouds from the CALIPSO satellite and from ground-based micropulse and Raman lidars. *J. Geophys. Res. Atmos.* **2013**, *118*, 9209–9220. [[CrossRef](#)]
25. Goldsmith, J.E.M.; Blair, F.H.; Bisson, S.E.; Turner, D.D. Turn-key Raman lidar for profiling atmospheric water vapor, clouds, and aerosols. *Appl. Opt.* **1998**, *37*, 4979–4990. [[CrossRef](#)]
26. Ferrare, R.; Turner, D.; Clayton, M.; Schmid, B.; Redemann, J.; Covert, D.; Elleman, R.; Ogren, J.; Andrews, E.; Goldsmith, J.E.M.; et al. Evaluation of daytime measurements of aerosols and water vapor made by an operational Raman lidar over the Southern Great Plains. *J. Geophys. Res. Atmos.* **2006**, *111*, D05S08. [[CrossRef](#)]
27. Newsom, R. Raman lidar (RL) handbook. In *Office of Scientific & Technical Information Technical Reports*; Citeseer: University Park, PA, USA, 2009.
28. Moran, K.P.; Martner, B.E.; Post, M.J.; Kropfli, R.A.; Welsh, D.C.; Widener, K.B. An Unattended Cloud-Profiling Radar for Use in Climate Research. *Bull. Am. Meteorol. Soc.* **1998**, *79*, 443–456. [[CrossRef](#)]
29. Clothiaux, E.E.; Miller, M.A.; Perez, R.C.; Turner, D.D.; Moran, K.P.; Martner, B.E.; Ackerman, T.P.; Mace, G.G.; Marchand, R.T.; Widener, K.B. *The ARM Millimeter Wave Cloud Radars (MMCRs) and the Active Remote Sensing of Clouds (ARSCL) Value Added Product (VAP)*; DOE Office of Science Atmospheric Radiation Measurement (ARM) User Facility; U.S. Department of Energy Office of Scientific and Technical Information: Oak Ridge, TN, USA, 2001.
30. Fu, Q.; Carlin, B.; Mace, G. Cirrus horizontal inhomogeneity and OLR bias. *Geophys. Res. Lett.* **2000**, *27*, 3341–3344. [[CrossRef](#)]
31. Carlin, B.; Fu, Q.; Lohmann, U.; Mace, G.G.; Sassen, K.; Comstock, J.M. High-Cloud Horizontal Inhomogeneity and Solar Albedo Bias. *J. Clim.* **2002**, *15*, 2321–2339. [[CrossRef](#)]
32. Widener, K.; Bharadwaj, N.; Johnson, K. *Ka-Band ARM Zenith Radar (KAZR) Instrument Handbook*; DOE Office of Science Atmospheric Radiation Measurement (ARM) Program; U.S. Department of Energy Office of Scientific and Technical Information: Oak Ridge, TN, USA, 2012.
33. Tinel, C.; Testud, J.; Pelon, J.; Hogan, R.J.; Protat, A.; Delanoë, J.; Bouniol, D. The Retrieval of Ice-Cloud Properties from Cloud Radar and Lidar Synergy. *J. Appl. Meteorol.* **2005**, *44*, 860–875. [[CrossRef](#)]
34. Borg, L.A.; Holz, R.E.; Turner, D.D. Investigating cloud radar sensitivity to optically thin cirrus using collocated Raman lidar observations. *Geophys. Res. Lett.* **2011**, *38*, L05807. [[CrossRef](#)]
35. Thorsen, T.J.; Fu, Q.; Newsom, R.K.; Turner, D.D.; Comstock, J.M. Automated Retrieval of Cloud and Aerosol Properties from the ARM Raman Lidar. Part I: Feature Detection. *J. Atmos. Ocean. Technol.* **2015**, *32*, 1977–1998. [[CrossRef](#)]

36. Thorsen, T.J.; Fu, Q. Automated Retrieval of Cloud and Aerosol Properties from the ARM Raman Lidar. Part II: Extinction. *J. Atmos. Ocean. Technol.* **2015**, *32*, 1999–2023. [[CrossRef](#)]
37. Fu, Q. An Accurate Parameterization of the Solar Radiative Properties of Cirrus Clouds for Climate Models. *J. Clim.* **1996**, *9*, 2058–2082. [[CrossRef](#)]
38. Fu, Q.; Liou, K.N. On the Correlated k-Distribution Method for Radiative Transfer in Nonhomogeneous Atmospheres. *J. Atmos. Sci.* **1992**, *49*, 2139–2156. [[CrossRef](#)]
39. Fu, Q.; Yang, P.; Sun, W.B. An Accurate Parameterization of the Infrared Radiative Properties of Cirrus Clouds for Climate Models. *J. Clim.* **1998**, *11*, 2223–2237. [[CrossRef](#)]
40. Rose, F.; Charlock, T. New Fu-Liou code tested with ARM raman lidar aerosols and CERES in pre-CALIPSO sensitivity study. In Proceedings of the 11th Conference on Atmospheric Radiation, Ogden, UT, USA, 3–7 June 2002.
41. Rose, F.; Charlock, T.; Fu, Q.; Kato, S.; Rutan, D.; Jin, Z. CERES proto-edition 3 radiative transfer: Model tests and radiative closure over surface validation sites. In Proceedings of the 12th Conference on Atmospheric Radiation, Madison, WI, USA, 9–14 July 2006.
42. Wu, X.; Balmes, K.A.; Fu, Q. Aerosol Direct Radiative Effects at the ARM SGP and TWP Sites: Clear Skies. *J. Geophys. Res. Atmos.* **2021**, *126*, e2020JD033663. [[CrossRef](#)]
43. Balmes, K.A.; Fu, Q. All-Sky Aerosol Direct Radiative Effects at the ARM SGP Site. *J. Geophys. Res. Atmos.* **2021**, *126*, e2021JD034933. [[CrossRef](#)]
44. Morris, V. *Microwave Radiometer (MWR) Handbook*; DOE Office of Science Atmospheric Radiation Measurement (ARM) Program; U.S. Department of Energy Office of Scientific and Technical Information: Oak Ridge, TN, USA, 2019.
45. Turner, D.D.; Vogelmann, A.M.; Austin, R.T.; Barnard, J.C.; Cady-Pereira, K.; Chiu, J.C.; Clough, S.A.; Flynn, C.; Khaiyer, M.M.; Liljegren, J.; et al. Thin Liquid Water Clouds: Their Importance and Our Challenge. *Bull. Am. Meteorol. Soc.* **2007**, *88*, 177–190. [[CrossRef](#)]
46. Dee, D.P.; Uppala, S.M.; Simmons, A.J.; Berrisford, P.; Poli, P.; Kobayashi, S.; Andrae, U.; Balmaseda, M.A.; Balsamo, G.; Bauer, P.; et al. The ERA-Interim reanalysis: Configuration and performance of the data assimilation system. *Q. J. R. Meteorol. Soc.* **2011**, *137*, 553–597. [[CrossRef](#)]
47. Yang, Q.; Fu, Q.; Austin, J.; Gettelman, A.; Li, F.; Vömel, H. Observationally derived and general circulation model simulated tropical stratospheric upward mass fluxes. *J. Geophys. Res. Atmos.* **2008**, *113*, D00B07. [[CrossRef](#)]
48. Roesch, A.; Schaaf, C.; Gao, F. Use of Moderate-Resolution Imaging Spectroradiometer bidirectional reflectance distribution function products to enhance simulated surface albedos. *J. Geophys. Res. Atmos.* **2004**, *109*, D12105. [[CrossRef](#)]
49. Schaaf, C.B.; Gao, F.; Strahler, A.H.; Lucht, W.; Li, X.; Tsang, T.; Strugnell, N.C.; Zhang, X.; Jin, Y.; Muller, J.-P.; et al. First operational BRDF, albedo nadir reflectance products from MODIS. *Remote Sens. Environ.* **2002**, *83*, 135–148. [[CrossRef](#)]
50. Heymsfield, A.; Winker, D.; Avery, M.; Vaughan, M.; Diskin, G.; Deng, M.; Mitev, V.; Matthey, R. Relationships between Ice Water Content and Volume Extinction Coefficient from In Situ Observations for Temperatures from 0° to –86 °C: Implications for Spaceborne Lidar Retrievals. *J. Appl. Meteorol. Clim.* **2014**, *53*, 479–505. [[CrossRef](#)]
51. Hong, Y.; Liu, G.; Li, J.-L.F. Assessing the Radiative Effects of Global Ice Clouds Based on CloudSat and CALIPSO Measurements. *J. Clim.* **2016**, *29*, 7651–7674. [[CrossRef](#)]
52. Ewald, F.; Groß, S.; Wirth, M.; Delanoë, J.; Fox, S.; Mayer, B. Why we need radar, lidar, and solar radiance observations to constrain ice cloud microphysics. *Atmos. Meas. Tech.* **2021**, *14*, 5029–5047. [[CrossRef](#)]